A Soft Microfabricated Capacitive Sensor for High Dynamic Range Strain Sensing

Hee-Sup Shin, Alexi Charalambides, Ivan Penskiy and Sarah Bergbreiter

***Abstract*— This work demonstrates an all-elastomer MEMS capacitive strain sensor with high dynamic range (5000:1), and features an inexpensive molding microfabrication process. The sensor is comprised of conductive elastometric comb capacitors embedded in a dielectric. Two different sensor designs, lateral combs (LC) and transverse combs (TC), were developed to evaluate sensor sensitivity as a function of load orientation. Both sensors have combs with a gap of 30 μm, length of 4 mm, and depth of 65 μm. A linear elastic analytical model was developed to predict change in capacitance as a function of strain, and experimental results show a reasonable agreement with the theoretical predictions. The observed strain responses have high linearity and dynamic range, and negligible hysteresis. The strain resolution of the LC and TC sensors is 100 μstrain and 500 μstrain, respectively, tested up to 50% strain.**

I. INTRODUCTION

The unique mechanical and electrical properties of soft-matter transducers allow them to be highly stretchable and flexible without compromising their electrical functionality. These properties are crucial for soft robotics, but also for flexible robotic components like joints in robot hands and legs that undergo high strains. Recent work has focused on soft sensors comprised of a silicone rubber or polydimethylsiloxane (PDMS). Stretchable conductors have the capability to measure external stresses even though they become highly deformed. Various types of stretchable conductors have been reported such as elastometric [1], [2], liquid [3], [4], and thin film conductors [5]–[7].

For this class of soft sensors, the electrical resistance or capacitance of elastomer conductors changes with deformation due to external loads. Using this, researchers have developed a variety of applications such as large deformation strain sensors [8], [9], tactile sensors [10]–[13], and wearable devices [14]–[16]. However, the majority of these sensors occupy a large area. Soft strain sensors that occupy small areas ($<$ 5 mm on a side) could be incorporated into small joints [17], soft pneumatic microactuators [18], or enable large numbers of sensors over a small area [19].

Liquid conductor-based sensors have been previously used to create flexible strain gauges [12]. However, even though sensors using liquid conductors show favorable mechanical and electrical properties [3], there are several limitations for miniaturization. One of the challenges is that the fabrication method to encase a liquid conductor is unfavorable for building microchannels with a cross-section of tens of microns. Specifically, a conductive liquid, such as eutectic indium gallium (eGaIn), is typically injected into a microchannel via a syringe, hence the microchannel is limited by the diameter of the syringe; the smallest inner diameter of a common syringe needle is 82.6 μm. In addition to this, as microfludic channels of the sensors have a smaller cross-section, injecting liquid conductors become more difficult because of their high surface tension and silicone rubbers' hydrophobic nature [20], [21].

All authors are with the Department of Mechanical Engineering and the Institute of System Research, University of Maryland, College Park. Author for correspondence: sarahb@umd.edu

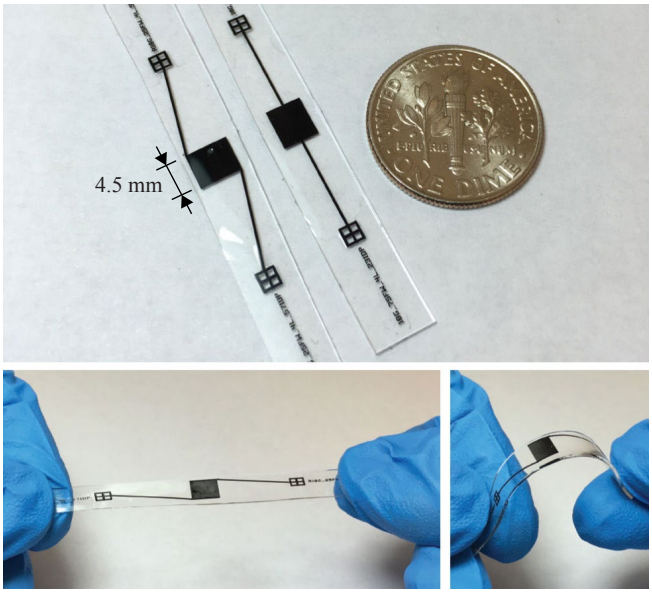

Fig. 1. Soft capacitive sensor samples exhibiting their stretchability and flexibility. The thickness of the sensors is 750 μm.

Conductive PDMS (cPDMS) composed of PDMS mixed with multi-walled carbon nanotubes (MWCNT or CNT) or other conductive particles is an alternative to microfluidic sensing due to favorable mechanical, thermal, and electrical properties [22]. Composites using MWCNTs have a 10 times lower percolation threshold in PDMS [23] compared to other particles, such as silver micropowder [1]. Because of its low percolation threshold, CNT/PDMS can sustain a high strain without losing much of its conductivity. Taking advantage of this characteristic, a variety of resistive strain sensors have been introduced [24], [25]. However, resistive sensors using conductive composites typically show a relatively high resistance hysteresis [24].

To address the above challenges without sacrificing dynamic range or size, an all-elastomer microfabricated capacitive strain sensor composed of CNT/PDMS combs embedded in PDMS is proposed (Fig. 1). By choosing a capacitive

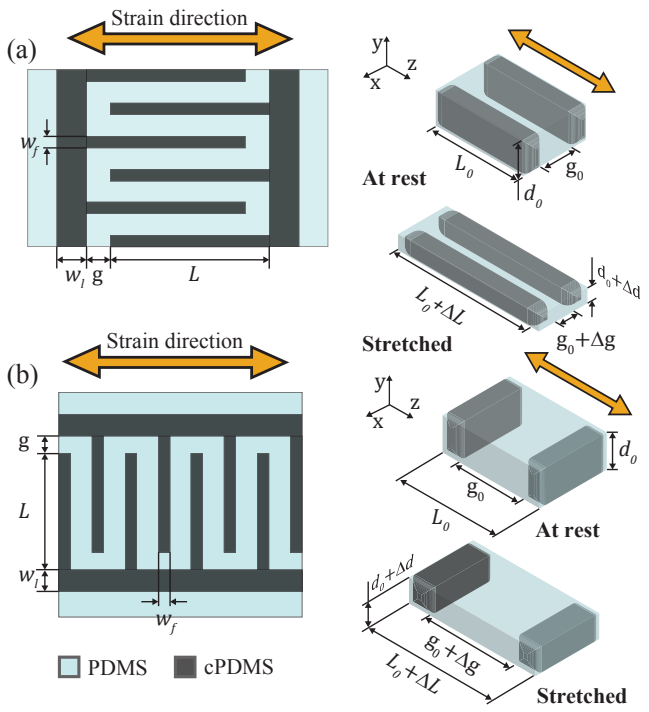

Fig. 2. Schematics of structures (left) and working principle (right) of the proposed sensor: (a) lateral comb (LC) and (b) transverse comb (TC).

transduction method, these sensors show high repeatability and hysteresis is limited to mechanical effects in the polymer. Microfabrication enables both compact size of sensors as well as large initial capacitance to improve the sensor's resolution and increase dynamic range. CNT/PDMS is selected over carbon black/PDMS used in previous work [26] to accommodate high strains without losing conductivity, and a relatively simple microfabrication process based on molding is used [10]. A linear elastic analytical model is developed and compared to the experimental results.

II. Sensor Design

The basic sensor design uses interdigitated capacitors (IDCs) [27], a relatively common architecture for a capacitive sensor in micro-electro-mechanical systems (MEMS). In the proposed soft sensor, cPDMS comb electrodes will be embedded in a PDMS dielectric to maintain flexibility and stretchability. This comb architecture increases the capacitance in a small area of sensor by meandering the gap between electrodes through the occupied area. As shown below, an increased initial capacitance results in greater sensor sensitivity.

The sensing principle of the introduced strain sensors is similar to typical soft sensors. Given an applied strain, the deformation of elastomeric sensor induces the cPDMS combs to be deformed along with the gaps between the neighboring comb electrodes, resulting in a change in capacitance. Different strain responses can be expected when different comb alignments are used, and specifically, two different comb architectures are employed: lateral and transverse combs [28]. As shown in Fig. 2(a), the lateral comb (LC) design employs comb electrodes in the direction parallel to the direction of strain. On the other hand, the transverse comb (TC) design uses electrodes orthogonally aligned to the strain direction, as shown in Fig. 2(b).

In the following analysis, the dimensions of both prototypes are g = 30 µm, w_f = 50 µm, and n = 49, where g is the size of gap between each fingers, w_f is the width of fingers, and n is the number of interdigitated gaps, respectively. The length and thickness of fingers, L and d, and the width of electrode leads, w_l is 4 mm, 65 µm and 250 µm, respectively. These parameters are also defined in Fig. 2.

A. Lateral comb (LC) sensor

The gaps between adjacent electrodes of the LC design decrease when the sensor is in uniaxial tension as shown in Fig. 2 (a). To better understand how these sensors will respond to strain, a simple parallel plate model is used as an initial modeling approach. However, based on the dimensions given above (specifically 30 µm gaps and 65 µm thickness), the sensor is only an approximation of a parallel plate. Based on a previously developed linear elastic model [29], the capacitance change of a single parallel plate (ΔC_p) can be expressed as:

$$\Delta C_p = \varepsilon_0 \varepsilon_r \frac{Ld}{g} \varepsilon_z, \tag{1}$$

where ε_0 and ε_r are vacuum and relative permittivity and ε_z is strain in z-axis (defined in Fig. 2).

Including the number of interdigitated gaps, n, in (1), the capacitance change of the sensor is defined by

$$\Delta C_{lc} = n\Delta C_p = n\varepsilon_0 \varepsilon_r \frac{Ld}{g} \varepsilon_z. \tag{2}$$

From the above expression, the normalized capacitance change of an LC-sensor is defined as

$$\Delta C_{lc}/C_0 = \varepsilon_z. \tag{3}$$

From (3), the strain response of LC-sensor depends solely on an applied strain. Sensitivity, S, however, is defined based on the initial capacitance, C_0.

$$S_{lc} = \Delta C_{lc}/\varepsilon_z = C_0 = n\varepsilon_0 \varepsilon_r \frac{Ld}{g} \tag{4}$$

If sensor resolution is defined as the noise equivalent signal ($\Delta C_{min} = \Delta C_{noise}/S$), resolution will improve as sensitivity is increased. Smaller gaps, large areas, and higher dielectric materials will all improve resolution and sensitivity in this sensor.

B. Transverse comb (TC) sensor

In the TC-sensor, the deformation of the combs is opposite to that of LC-sensor. The applied uniaxial strain results in the two electrodes moving further away from each other, causing a decrease in capacitance. Similar to the analytical model of

LC-sensor, the normalized capacitance change of TC-sensor can be described as

$$\Delta C_{tc}/C_0 = \frac{(1-\nu\varepsilon_z)^2}{1+\varepsilon_z} - 1, \quad (5)$$

where Poisson's ratio, ν, is 0.5 with the assumption that PDMS is an incompressible material. By using a linear fit of the TC sensor's sensitivity, it is found that S_{tc} is also proportional to the initial capacitance, but decreases as strain is applied.

$$\Delta S_{tc} = C_0\{\frac{(1-\nu\varepsilon_z)^2}{1+\varepsilon_z} - 1\}/\varepsilon_z \approx C_0(1.95\varepsilon_z - 2) \quad (6)$$

From (3) and (5), the 10.53 pF of initial capacitance of both sensors is obtained with the relative permittivity of PDMS, ε_r=2.8 [30]. Gauge factor (GF) is used as a normalized version of sensor sensitivity for comparison to commercial resistive strain sensors, GF = $\Delta C/(C_0\varepsilon)$. Up to 20 % strain, the calculated GF of LC- and TC-sensor are 1 and -1.62, respectively. Due to the nonlinearity of TC-sensor's analytical model, linear fitting was used for calculating GF. From the obtained GFs, we can expect that TC-sensor shows higher sensitivity.

III. Fabrication

The sensors were fabricated using a process developed in previous work [10] by casting cPDMS in a microfabricated mold, as shown in Fig. 3. The microfabrication of the mold began with depositing 0.6 µm silicon dioxide (SiO_2) on a 100 mm silicon wafer, followed by spinning and patterning a photoresist with standard lithography. In step (b), a 6:1 buffered hydrofluoric acid (BHF) etch of SiO_2 layer was performed to define the hard mask, followed by a deep reactive ion etch (DRIE) to create the final structure of the mold shown in Fig. 4. In step (c), the patterned photoresist was stripped off by oxygen (O_2) plasma and then the mold was silanized using vacuum deposition of trichlorosilane (Sigma-Aldrich, 448931) to prevent adhesion of cured cPDMS to the mold. At this point, the mold is ready to fabricate sensors and is reusable.

Sensors were then fabricated by molding cPDMS and coating it with PDMS. cPDMS (7 wt.% MWCNT) was prepared by mixing 0.0828 g of MWCNTs powder [1] and 1 g of PDMS (Sylgard 184, Dow Corning) mixed at a 10:1 curing ratio. Mixing was performed in a centrifugal mixer at 2000 rpm (Thinky, ARE-310). In step (d), cPDMS was cast by hand using an industrial screen printing squeegee (Ryonet), refilling the traces with the prepared cPDMS paste. Next, the cPDMS paste in the mold was degassed in a desiccator for 15 min, and then planarized by the squeegee again. The planarized cPDMS was cured on a hot plate for 12 min at 120°C. Due to the imperfect planarization, some cPDMS residue in between the combs was left behind. These electrical shorts, or "bridges", were removed by scrapping the surface of the mold using a razor blade and rinsed with

[1]MWCNTs powder: 10−20 nm of outer diameter and 10−30 µm length (Cheap Tubes Inc.)

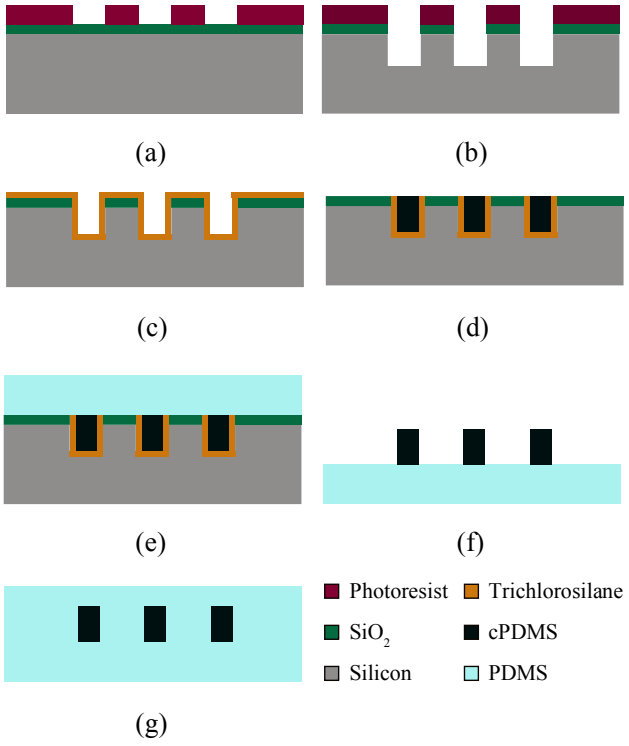

Fig. 3. Microfabrication process: (a) Deposit silicon dioxide (SiO_2) and then pattern photoresist. (b) 6:1 BHF etch SiO_2 layer and DRIE Si wafer. (c) Vacuum-deposit trichlorosilane. (d) Refill, planarize, and cure cPDMS and clean cPDMS residuals. (e) Coat with PDMS. (f) Peel off devices. (g) Cover sensing areas with PDMS.

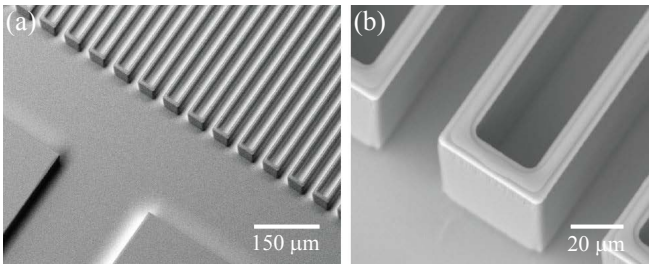

Fig. 4. Scanning electron microscopy (SEM) images of (a) the mold and (b) the close-up view of the trenches.

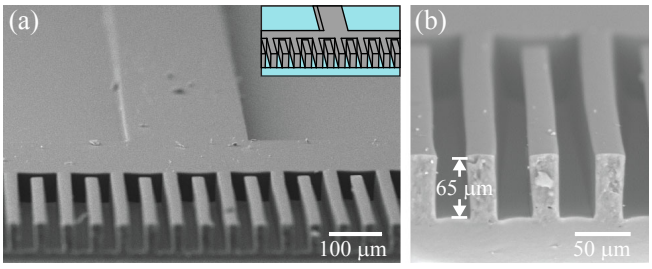

Fig. 5. SEM images of (a) a sensor structure and (b) its cross-setion. The inset of (a) depicts cPDMS comb and electrical lead (gray) and PDMS sheet (blue).

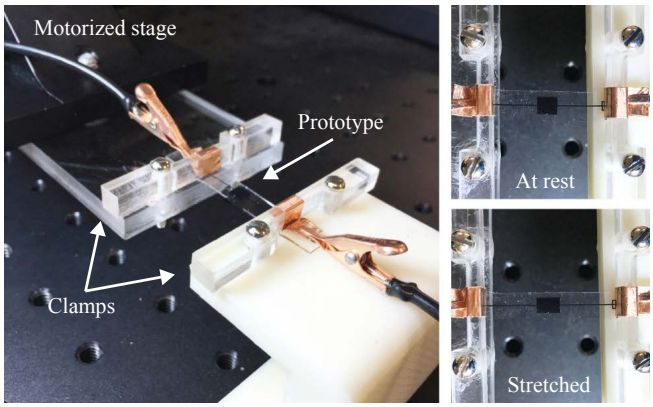

Fig. 6. Uniaxial strain experiment setup for sensor characterization. Close-up view of a sensor sample (top right) before and (bottom right) after being stretched.

isopropyl alcohol. In step (e), liquid PDMS was poured on the mold, vacuumed for 12 min, and cured on a hot plate for 12 min at 120°C. In step (f), the cured PDMS substrate was peeled off from the mold. The actual sensor structure obtained in this step is shown in Fig. 5. Finally, the sensing area and electrical leads were coated with PDMS to fully encapsulate the sensor in step (g).

IV. Characterization

Fig. 6 shows the experimental setup for two different types of strain tests: uniaxial static strain and dynamic strain. A motorized translation stage (PT3-Z8, Thorlabs) was used for applying uniaxial strains. In addition to this, the capacitance change of the prototypes was measured by using an evaluation board (EVAL-AD7745/46EB, Analog Devices) at a sampling rate of 16.1 Hz. Based on 500 data samples, the measured capacitance of the LC-sensor and the TC-sensor at rest was 17.00 pF and 16.15 pF, and the peak-to-peak noise (p-p noise) of each sensor was 1.6 fF and 12.4 fF, respectively.

A. Static Strain Response

The strain responses of the prototypes were measured by applying uniaxial strains. Each measurement was performed by applying strain in various increments depending on the test. For microstrain tests, 100 $\mu\varepsilon$ and 500 $\mu\varepsilon$ increments were used for the LC-sensor and TC-sensor, respectively. Increments of 1 % strain were used for both sensors to test large strain responses. After incrementing the strain applied to the sensor, the stage was paused for 3 seconds to measure the capacitance change of the sensors.

In order to characterize the resolution of the LC-sensor, strains up to 500 $\mu\varepsilon$ with increments of 100 $\mu\varepsilon$ were applied. Here, the increment was decided by the minimum detectable strain based on the measured p-p noise. The inset of Fig. 7(a) shows the response of the sensor. Due to the relatively low p-p noise, approximately uniform standard deviation (SD) bars were shown in Fig. 7(a). These standard deviations are based on multiple tests of the same sensor. As expected from Eq. 3, the strain response was linear. Based on linear fitting of

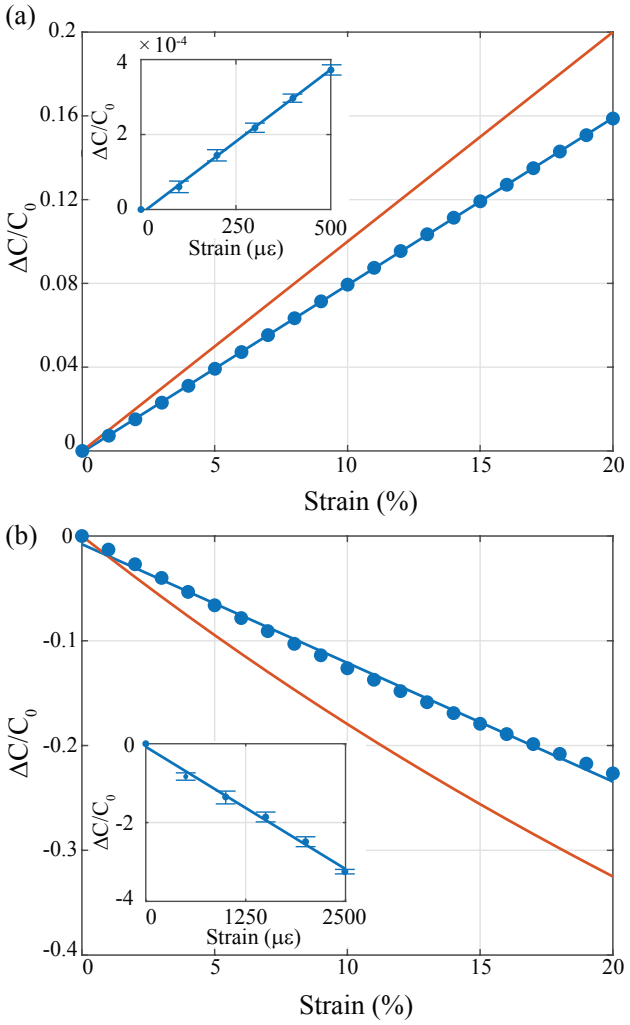

Fig. 7. Static strain response of (a) LC-sensor and (b) TC-sensor: blue line, mark and bar denotes the linear fit, the mean value and the standard deviation of acquired samples, respectively. Orange line stands for theoretical expectation.

data, the GF was 0.77. In addition to this, the dynamic range is defined by $\varepsilon_H/\varepsilon_L$, where ε_H and ε_L are the highest and lowest strain the sensor can measure. Based on the resolution of LC-sensor and a maximum strain of 50% measured in the dynamic tests below, the dynamic range (DR) of the LC-sensor is 5000.

The responses of the LC-sensor to large strain and its theoretical prediction is presented in Fig. 7(a). Similar to the microstrain response, the sensor signal was approximately linear. Also, the trend of the sensor response and the theoretical expectation showed the reasonable agreement, though 20% error was observed. In addition to this, the gauge factor at larger strains (up to 0.2 ε) was slightly higher than that at small strains ($\leq$ 500 $\mu\varepsilon$). Based on linear fitting, the calculated GF of the large strain response was 0.80.

In contrast to the LC-sensor, the high p-p noise of the TC-sensor compromised the sensor's capability to measure microstrain, as shown in the inset of Fig. 7(b). Compared

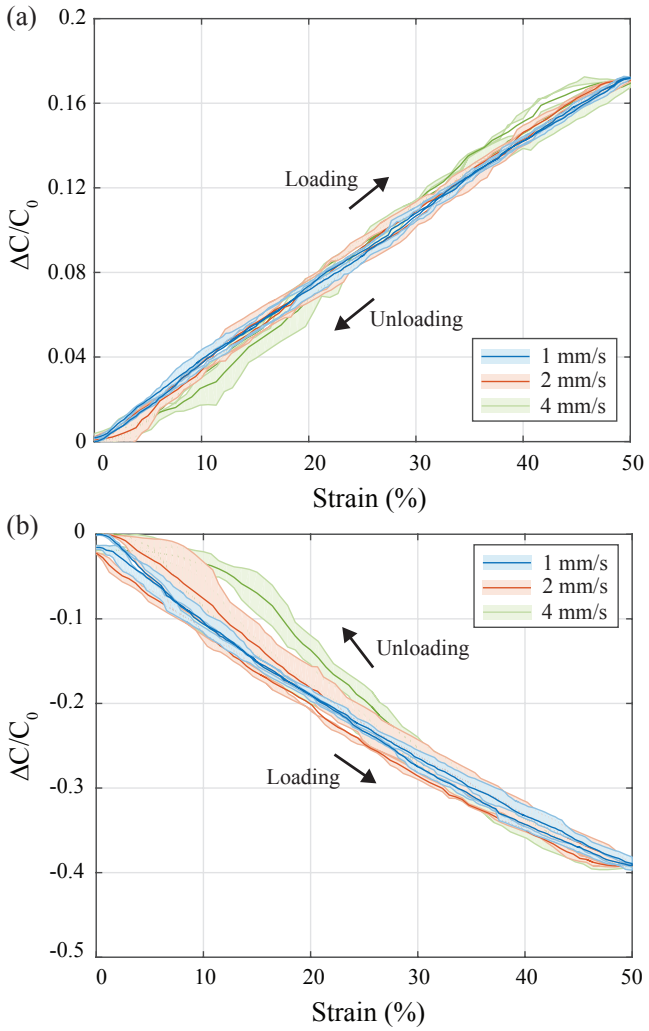

Fig. 8. Dynamic strain responses of (a) LC-sensor and (b) TC-sensor with different rates (1 mm/sec, 2 mm/sec, and 4 mm/sec). Color bands and solid lines denote the standard deviation and mean values of three trials, respectively.

to the microstrain response of the LC-sensor, a relatively low resolution of the sensor, 500 $\mu\varepsilon$, was measured. From linear fitting, The measured GF of the TC-sensor was -1.24 at small strains. Given the same maximum strain of 50%, a dynamic range of 1000 was calculated from the resolution of TC-sensor.

In the case of large strain, the TC-sensor showed an approximately linear response in both experimental results and theoretical expectations as shown in Fig 7(b). Compared to the LC-sensor case, a higher error (30 %) between the experimental result and the theoretical expectation was observed. To calculate GF, linear fitting was used and the GF of experimental result was -1.13. Opposite to the LC-sensor case, the GF decreased in the large strain response in comparison to the GF at small strains.

B. Dynamic Strain Response

To characterize the dynamic strain response of the sensor samples, each sensor prototype was stretched and returned to its original position at different rates (1 mm/sec, 2 mm/sec, and 4 mm/sec) with a maximum strain of 50 %. Three trials at each rate were used to investigate the repeatability of the sensors.

TABLE I

COMPARISON OF THEORETICAL PREDICTIONS AND EXPERIMENTAL RESULTS OF LC- AND TC-SENSOR.

		LC-sensor	TC-sensor
Theory	Gauge Factor	1	-1.62
	Initial capacitance (pF)	10.53	10.53
Experiment	Gauge Factor	0.80	-1.13
	Initial capacitance (pF)	17	16.15
	Resolution ($\mu\varepsilon$)	100	500
	Dynamic Range	5000	1000

Experimental results for the LC-sensor are presented in Fig. 8(a). The sensor sample displayed a highly linear strain response, regardless of the loading and unloading rates. In addition to this, the prototype shows repeatable responses as well as low hysteresis (defined by the difference between the stretch and return curves).

Similar to the experimental results of the LC-sensor, the strain response of the TC-sensor was approximately linear and repeatable as shown in Fig. 8(b). Likewise, the hysteresis of the sensor was small. However, the prototype showed a higher hysteresis level than that of the LC-sensor when a loading/unloading rate of 4 mm/sec was used.

V. DISCUSSION

The results demonstrate the proposed sensors' high dynamic range with a linear, sensitive, and repeatable response. The primary contribution of these sensor designs is their compact size and high resolution without compromised stretchability. Table I reiterates the results obtained in previous sections.

The LC-sensor has a resolution 5 times higher than the TC-sensor. As discussed previously, resolution is defined as the noise divided by the sensor sensitivity. This result is not surprising then given that the LC-sensor has a higher initial capacitance and lower p-p noise, although it is still unclear where this higher level of noise comes from. Despite the fact that the initial capacitance of the sensors should be identical as designed, fabrication tolerances will result in differences similar to those measured.

The experimental results verified the TC-sensor's higher GF as predicted by analytical models. Based on the experimental results, the GF of the TC-sensor is 1.4 times higher than the GF of the LC-sensor. Given the applied strain, the gaps of the TC-sensor experience larger deformation than those of the LC-sensor, causing larger changes in capacitance. Hence, the TC-sensor is capable of having higher sensitivity and lower resolution as compared to the LC-sensor. However, the larger deformation of the gaps results in a higher hysteresis level compared to LC-sensor. In the dynamic strain tests, higher hysteresis in both sensors was observed as a higher loading and unloading rate was used. This is due to viscoelastic characteristics of PDMS

that hinder the sensor from quickly recovering its original shape. This effect was more clearly seen in TC-sensor case because of the larger deformation of its gaps. Nevertheless, the hysteresis level of TC-sensor were still small.

Due to the limited capacitance range of the evaluation board ($\pm$4 pF), the sensor prototypes were only tested up to 50 % of strain in this work. However, the prototypes are expected to be able to operate as far as 120 % of strain, based on the ultimate elongation of PDMS and cPDMS [23], [31], and remains a subject of future work.

In addition to the promising results of these sensor prototypes, there are a few challenges that need to be dealt with for our proposed prototype to be more practical. In the theoretical and experimental results, it is assumed that the applied strain direction is known a priori. However, if the strain direction is unknown, a single sensor will not be able to differentiate the strain direction. In order to enable the sensor to distinguish different kinds of strains, developing more complex architectures will be a subject of future work.

The current fabrication method does not always guarantee a completely cleaned surface after casting the cPDMS, as shown in Fig. 9. As mentioned in the fabrication section, the cleaning process is manually performed, hence, the yields rely mainly on the ability of technicians. In addition, removing bridges spanning smaller electrode gaps is more difficult, thereby making it more challenging to either increase the number of interdigitated pairs in same size of sensing area or reduce the sensor size while maintaining sensitivity. Also, as features of gaps in the mold are made smaller, they are more vulnerable to external force due to their high aspect ratio. One possible solution is to improve cleaning techniques by using techniques for etching PDMS, such as laser etching [32], tetrabutylammonium fluoride (TBAF) and n-methylpyrrolidone (NMP) wet etching [33], and CF_4 and O_2 plasma etching [33], [34]. Further investigation on more reliable cleaning processes based on the above techniques will be an immediate future research area.

Furthermore, the current analytical models rely only on simple linear elastic and parallel plate capacitor models, and can therefore not take account of the hyperelastic behavior of elastomers at large strains and neglect fringing fields from the top and bottom surfaces of electrodes. This may be part of the reason the theoretical predictions deviated from experimental results. Improved analytical models will provide a more accurate prediction of sensor response. In addition, using finite element analysis (FEA) to predict the deformation shape of the combs as well as the strain response of the sensor will be important to improving this analytical predictive model.

VI. Conclusion

The primary contribution of this work is to introduce a compact size soft capacitive strain sensor composed of cPDMS comb drives embedded in a single PDMS film, along with their analytical and experimental characterization. The theoretical models were validated with experimental measurements. The predictions of the analytical models and experimental results confirmed the proposed prototype's favorable functionalities. In particular, the prototypes showed high initial capacitance, linearity, and dynamic range that cannot be achieved from typical metal foil or flexible strain gauges. Furthermore, these unique characteristics including negligible hysteresis allow the sensor promising to be integrated with a variety of robotic applications.

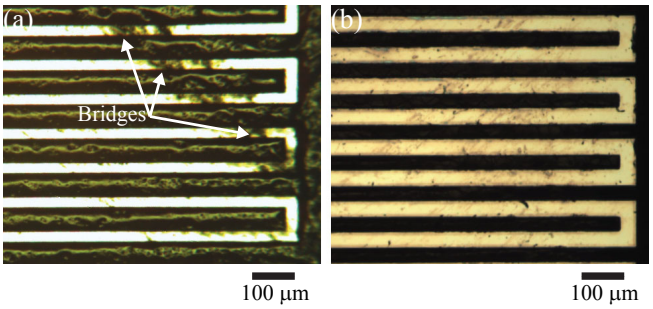

Fig. 9. Microscopic image of the mold filed with cPDMS (a) before and (b) after cleaning process.

Acknowledgment

This work was supported by the Nature-inspired Flight Technologies+Ideas (NIFTI) AFOSR Center of Excellence. The authors acknowledge the support of the Maryland NanoCenter and its FabLab.

References

[1] X. Niu, S. Peng, L. Liu, W. Wen, and P. Sheng, "Characterizing and patterning of pdms-based conducting composites," *Advanced Materials*, vol. 19, no. 18, p. 2682, 2007.

[2] M. Moniruzzaman and K. I. Winey, "Polymer nanocomposites containing carbon nanotubes," *Macromolecules*, vol. 39, no. 16, pp. 5194–5205, 2006.

[3] M. D. Dickey, R. C. Chiechi, R. J. Larsen, E. A. Weiss, D. A. Weitz, and G. M. Whitesides, "Eutectic gallium-indium (egain): A liquid metal alloy for the formation of stable structures in microchannels at room temperature," *Advanced Functional Materials*, vol. 18, no. 7, pp. 1097–1104, 2008.

[4] T. Liu, P. Sen, and C.-J. C. Kim, "Characterization of nontoxic liquid-metal alloy galinstan for applications in microdevices," *Microelectromechanical Systems, Journal of*, vol. 21, no. 2, pp. 443–450, 2012.

[5] D. J. Lipomi, M. Vosgueritchian, B. C. Tee, S. L. Hellstrom, J. A. Lee, C. H. Fox, and Z. Bao, "Skin-like pressure and strain sensors based on transparent elastic films of carbon nanotubes," *Nature nanotechnology*, vol. 6, no. 12, pp. 788–792, 2011.

[6] W. M. Choi, J. Song, D.-Y. Khang, H. Jiang, Y. Y. Huang, and J. A. Rogers, "Biaxially stretchable "wavy" silicon nanomembranes," *Nano Letters*, vol. 7, no. 6, pp. 1655–1663, 2007.

[7] D.-Y. Khang, H. Jiang, Y. Huang, and J. A. Rogers, "A stretchable form of single-crystal silicon for high-performance electronics on rubber substrates," *Science*, vol. 311, no. 5758, pp. 208–212, 2006.

[8] A. Fassler and C. Majidi, "Soft-matter capacitors and inductors for hyperelastic strain sensing and stretchable electronics," *Smart Materials and Structures*, vol. 22, no. 5, p. 055023, 2013.

[9] S. Jang and H. Yin, "Effect of aligned ferromagnetic particles on strain sensitivity of multi-walled carbon nanotube/polydimethylsiloxane sensors," *Applied Physics Letters*, vol. 106, no. 14, p. 141903, 2015.

[10] A. Charalambides and S. Bergbreiter, "A novel all-elastomer mems tactile sensor for high dynamic range shear and normal force sensing," *Journal of Micromechanics and Microengineering*, vol. 25, no. 9, p. 095009, 2015.

[11] P. D. Block and S. Bergbreiter, "Large area all-elastomer capacitive tactile arrays," in *SENSORS, 2013 IEEE*. IEEE, 2013, pp. 1–4.

[12] Y.-L. Park, B.-R. Chen, and R. J. Wood, "Design and fabrication of soft artificial skin using embedded microchannels and liquid conductors," *Sensors Journal, IEEE*, vol. 12, no. 8, pp. 2711–2718, 2012.

[13] J.-B. Chossat, H.-S. Shin, Y.-L. Park, and V. Duchaine, "Soft tactile skin using an embedded ionic liquid and tomographic imaging," *Journal of Mechanisms and Robotics*, vol. 7, no. 2, p. 021008, 2015.

[14] J.-B. Chossat, Y. Tao, V. Duchaine, and Y.-L. Park, "Wearable soft artificial skin for hand motion detection with embedded microfluidic strain sensing," in *Robotics and Automation (ICRA), 2015 IEEE International Conference on*. IEEE, 2015, pp. 2568–2573.

[15] R. K. Kramer, C. Majidi, and R. J. Wood, "Wearable tactile keypad with stretchable artificial skin," in *Robotics and Automation (ICRA), 2011 IEEE International Conference on*. IEEE, 2011, pp. 1103–1107.

[16] J.-H. Moon, D. H. Baek, Y. Y. Choi, K. H. Lee, H. C. Kim, and S.-H. Lee, "Wearable polyimide–pdms electrodes for intrabody communication," *Journal of Micromechanics and Microengineering*, vol. 20, no. 2, p. 025032, 2010.

[17] R. J. Wood, "The first takeoff of a biologically inspired at-scale robotic insect," *Robotics, IEEE Transactions on*, vol. 24, no. 2, pp. 341–347, 2008.

[18] M. De Volder and D. Reynaerts, "Pneumatic and hydraulic microactuators: a review," *Journal of Micromechanics and microengineering*, vol. 20, no. 4, p. 043001, 2010.

[19] A. Eberle, B. Dickerson, P. Reinhall, and T. Daniel, "A new twist on gyroscopic sensing: body rotations lead to torsion in flapping, flexing insect wings," *Journal of The Royal Society Interface*, vol. 12, no. 104, p. 20141088, 2015.

[20] Y.-L. Park, D. Tepayotl-Ramirez, R. J. Wood, and C. Majidi, "Influence of cross-sectional geometry on the sensitivity and hysteresis of liquid-phase electronic pressure sensors," *Applied Physics Letters*, vol. 101, no. 19, p. 191904, 2012.

[21] H.-S. Shin, J. Ryu, C. Majidi, and Y.-L. Park, "Enhanced performance of microfluidic soft pressure sensors with embedded solid microspheres," *Journal of Micromechanics and Microengineering*, vol. 26, no. 2, p. 025011, 2016.

[22] R. Khare and S. Bose, "Carbon nanotube based composites-a review," *Journal of minerals and Materials Characterization and Engineering*, vol. 4, no. 01, p. 31, 2005.

[23] J. Lu, M. Lu, A. Bermak, and Y.-K. Lee, "Study of piezoresistance effect of carbon nanotube-pdms composite materials for nanosensors," in *Nanotechnology, 2007. IEEE-NANO 2007. 7th IEEE Conference on*. IEEE, 2007, pp. 1240–1243.

[24] C.-X. Liu and J.-W. Choi, "Strain-dependent resistance of pdms and carbon nanotubes composite microstructures," *Nanotechnology, IEEE Transactions on*, vol. 9, no. 5, pp. 590–595, 2010.

[25] C. Lee, L. Jug, and E. Meng, "High strain biocompatible polydimethylsiloxane-based conductive graphene and multiwalled carbon nanotube nanocomposite strain sensors," *Applied Physics Letters*, vol. 102, no. 18, p. 183511, 2013.

[26] A. P. Gerratt, M. Tellers, and S. Bergbreiter, "Soft polymer mems," in *Micro Electro Mechanical Systems (MEMS), 2011 IEEE 24th International Conference on*. IEEE, 2011, pp. 332–335.

[27] R. Igreja and C. Dias, "Analytical evaluation of the interdigital electrodes capacitance for a multi-layered structure," *Sensors and Actuators A: Physical*, vol. 112, no. 2, pp. 291–301, 2004.

[28] R. Matsuzaki and A. Todoroki, "Wireless flexible capacitive sensor based on ultra-flexible epoxy resin for strain measurement of automobile tires," *Sensors and Actuators A: Physical*, vol. 140, no. 1, pp. 32–42, 2007.

[29] D. J. Cohen, D. Mitra, K. Peterson, and M. M. Maharbiz, "A highly elastic, capacitive strain gauge based on percolating nanotube networks," *Nano letters*, vol. 12, no. 4, pp. 1821–1825, 2012.

[30] J. Brandrup, E. H. Immergut, E. A. Grulke, A. Abe, and D. R. Bloch, *Polymer handbook*. Wiley New York, 1999, vol. 89.

[31] I. Johnston, D. McCluskey, C. Tan, and M. Tracey, "Mechanical characterization of bulk sylgard 184 for microfluidics and microengineering," *Journal of Micromechanics and Microengineering*, vol. 24, no. 3, p. 035017, 2014.

[32] D. J. Cappelleri, G. Piazza, and V. Kumar, "A two dimensional vision-based force sensor for microrobotic applications," *Sensors and Actuators A: Physical*, vol. 171, no. 2, pp. 340–351, 2011.

[33] B. Balakrisnan, S. Patil, and E. Smela, "Patterning pdms using a combination of wet and dry etching," *Journal of Micromechanics and Microengineering*, vol. 19, no. 4, p. 047002, 2009.

[34] J. Garra, T. Long, J. Currie, T. Schneider, R. White, and M. Paranjape, "Dry etching of polydimethylsiloxane for microfluidic systems," *Journal of Vacuum Science & Technology A*, vol. 20, no. 3, pp. 975–982, 2002.